COMPUTATIONAL ASPECTS OF THE PREDICTION OF MULTIDIMENSIONAL TRANSONIC FLOWS IN TURBOMACHINERY

By David A. Oliver and Panagiotis Sparis
Massachusetts Institute of Technology

INTRODUCTION

The analytical prediction and description of transonic flow in turbomachinery is complicated by three fundamental effects: (1) The fluid equations describing the transonic regime are inherently nonlinear, (2) shock waves may be present in the flow, and (3) turbo-machine blading is geometrically complex, possessing large amounts of curvature, stagger, and twist. Simple analytically separable solutions are therefore not readily obtainable. (The complex geometry of a typical transonic compressor rotor is shown in fig. 1.) Because of these analytical difficulties, a computational approach to the prediction and design of transonic turbomachine flows is strongly warranted.

In the present work, a three-dimensional computation procedure for the study of transonic turbomachine fluid mechanics is described. The fluid differential equations and corresponding difference operators are presented, the boundary conditions for complex blade shapes are described, and the computational implementation and mapping procedures are developed. Illustrative results of a typical unthrottled transonic rotor are also presented.

FLUID EQUATIONS AND DIFFERENCE OPERATORS

The densities of mass ρ, momenta m_i, and energy e defined by the fluid state vector $\underline{U}(x_i, t)$ are governed by the fluid conservation laws in cylindrical coordinates $\left(x_1 = r, \ x_2 = \theta, \text{ and } x_3 = z\right)$ and time t:

$$\frac{\partial \underline{U}}{\partial t} = \frac{1}{r}\left[\frac{\partial \underline{F}_i}{\partial x_i} + \underline{K}(\underline{U})\right] \tag{1}$$

In a coordinate system fixed to a turbomachine blade rotating at angular velocity Ω, the state vector $\underline{U}$, and the flux vectors $\underline{F}_i(\underline{U})$ and $\underline{K}(\underline{U})$ are

$$\underline{U} = \left[\rho, \rho u_r, \rho u_\theta, \rho u_z, e\right] \tag{2}$$

18

$$\underline{F}_1 = r \begin{vmatrix} \rho u_r \\ \rho u_r^2 + p \\ \rho u_r u_\theta \\ \rho u_r u_z \\ (e + p)u_r \end{vmatrix} \qquad \underline{F}_2 = \begin{vmatrix} \rho(u_\theta - r\Omega) \\ \rho u_r(u_\theta - r\Omega) \\ \rho u_\theta(u_\theta - r\Omega) + p \\ \rho u_z(u_\theta - r\Omega) \\ (e + p)(u_\theta - r\Omega) \end{vmatrix} \qquad (3a)$$

$$\underline{F}_3 = r \begin{vmatrix} \rho u_z \\ \rho u_r u_z \\ \rho u_r u_\theta \\ \rho u_z^2 + p \\ (e + p)u_z \end{vmatrix} \qquad \underline{K} = \begin{vmatrix} 0 \\ \rho u_\theta^2 + p \\ \rho u_r u_\theta \\ 0 \\ 0 \end{vmatrix} \qquad (3b)$$

In equations (3), the pressure p appears which is expressed in terms of the state vector $\underline{U}$ through the equation of state.

A time-explicit difference operator S approximating the fluid equations (eq. (1)) with second-order accuracy coupled with a local stabilizing operator D is used to advance the fluid state from time level n to level $n + 1$ over the interval δt as follows:

$$\underline{U}^{n+1} = (S + D)\underline{U}^n \qquad (4)$$

Here, following MacCormack (ref. 1), S is formed in two steps as

$$\underline{U}^* = -\frac{1}{r}\left[\frac{\delta t}{\delta x_i} \Delta_i^+ \underline{F}_i(\underline{U}) + \delta t \underline{K}(\underline{U})\right]$$

$$S\underline{U} = \frac{1}{2}\left\{\underline{U}^* + \underline{U} - \frac{1}{r}\left[\frac{\delta t}{\delta x_i} \Delta_i^- \underline{F}_i(\underline{U}^*) + \delta t \underline{K}(\underline{U}^*)\right]\right\} \qquad (5)$$

The operators Δ_i^+ and Δ_i^- are the forward and backward difference operators in the coordinate directions x_i:

$$\Delta^+ f(x) = f(x + \delta x) - f(x)$$

$$\Delta^- f(x) = f(x) - f(x - \delta x) \qquad (6)$$

If the difference operator (eq. (5)) is applied successively in split steps (ref. 2) for each coordinate direction, the numerical stability conditions are

$$\delta t \leq \underset{i}{\text{Min}} \left\{ \frac{\delta x_i}{|u_i| + c} \right\} \tag{7}$$

At stagnation points or sonic points, the linearized version of the difference operator (eq. (5)) is neutrally stable independently of the choice of $\delta t/\delta x_i$. For a genuinely linear difference operator this occurrence is of no consequence and stable solutions of the difference equations can be achieved. In the nonlinear case, however, the true stability of the operator at the neutral point will be determined by the higher order nonlinear terms, and these terms will destabilize the difference operator. This numerical instability is an inherently numerical instability induced by higher order terms in the truncation error. Hence the nonlinear difference operator may be stabilized by the introduction of an artificial dissipation term of the order of the truncation error of the difference operator. In the case of the difference operator (eq. (5)), this term must be of third order in $\delta t, \delta x_i$.

The global damping or stabilizing operator D_0 may be summarized in the archetypal form

$$D_0 \underline{U} = \kappa \, \frac{\delta t}{\delta x_i} \frac{\Delta_i^+ Q \Delta_i^- + \Delta_i^- Q \Delta_i^+}{2} \, \underline{U} \tag{8}$$

where $Q(\underline{U})$ is a matrix diffusion coefficient of order $\delta t, \delta x_i$ and κ is an order unity nondimensional constant. A Taylor's series expansion of this operator shows that it is the difference expression for the continuous diffusion operator

$$\kappa \delta x_i^2 \, \frac{\delta t}{\delta x_i} \frac{\partial}{\partial x_i} \, Q \, \frac{\partial \underline{U}}{\partial x_i} \tag{9}$$

The neutral stability condition of the linearized operator occurs at sonic points and stagnation points. While a sonic point exists in the interior of a shock wave, the nonlinear instability could be just as important in smooth isentropic regions of transonic flow passing continuously through the sonic point as in regions where shocks are present. Calculations performed with the operator (eq. (5)) have confirmed this conjecture. For subsonic flows up into the high subsonic regime, the undamped operators have been demonstrated to be stable. However, where the Mach number was increased into the transonic regime, numerical instabilities occurred which could be eliminated with the use of the damping operator.

On the basis of the observations, the nonlinear instability should be confined to those regions of the flow where the eigenvalues of the amplification matrix are unity, i.e., at sonic and stagnation points. The damping operator D should then be structured such

that it becomes significant only near the sonic and stagnation points and not operative in other portions of the flow. A damping operator with such characteristics is

$$D = f(M)D_0 \tag{10}$$

where $f(M)$ is a distribution function which depends upon the local Mach number such that $f(M) = 1$ for $M = 0$ or $M = 1$, but $f(M) \ll 1$ for $M \neq 0$ and 1. A useful function with such properties is the Lorentz Line shape function

$$f(M) = \frac{1}{1 + \left(\dfrac{M - 1}{\Delta M}\right)^2} + \frac{1}{1 + \left(\dfrac{M}{\Delta M}\right)^2} \tag{11}$$

where the parameter ΔM represents the effective width in Mach number of the distribution function which peaks at $M = 0$ and 1. The use of the local damping operator D in place of the global operator D_0 can offer significant improvement in the resolution of the flow while maintaining stability of the difference operator.

The utility of the local damping operator is shown in figure 2 where the supercritical transonic flow of a $\gamma = 1.4$ gas over a right circular cylinder has been computed. This calculation was performed with a minimal number of mesh points (20) distributed over the surface of the half-cylinder to test the utility of the local damping operator. Significant improvement of the flow-field resolution, including the shock wave, results.

BOUNDARY CONDITIONS ON BLADE SURFACES

The appropriate boundary condition on an impenetrable blade surface for an inviscid flow is the single condition

$$u_n = 0 \tag{12}$$

where u_n is the velocity normal to the blade surface in blade coordinates. This boundary condition is not readily implemented in the finite-difference procedures described in the previous section because the full fluid state $\underline{U}$ is required at each point including the boundary points. If, as in figure 3, the boundary points are treated as interior points to which the difference equation (eq. (5)) is to be applied, then the application of the boundary condition, which consists of the determination of the state vector $\underline{U}$ at the auxiliary point, must be such that only the single condition (eq. (12)) is imposed at the blade surface.

If Σ is the surface of a sufficiently smooth three-dimensional body, then at each point M on the surface Σ a triply orthogonal curvilinear coordinate system may be defined consisting of the local normal ζ to the surface Σ at the point M and two curves of the surface $\Sigma(\eta$ and $\xi)$ that are normal to each other at the point M. If dn, dτ, and ds are the differential arc lengths along the axes ξ, η, and ζ, respectively, then

$$\left.\begin{array}{l} ds = h_s \, d\xi \\[2mm] d\tau = h_T \, d\eta \\[2mm] dn = h_n \, d\zeta \end{array}\right\} \tag{13}$$

The equations of motion may be expressed in the curvilinear coordinate system ξ, η, and ζ. By introducing the boundary condition $u_n = 0$ and the radii of curvature R_s and R_T of the surface Σ in the direction of the axes ξ and η, the equations of motion may be written in the following form, correct only for points on the surface Σ (ref. 3):

$$\frac{\partial \rho}{\partial t} + \frac{1}{h_s h_T}\left[\frac{\partial}{\partial \xi}\left(h_T u_s \rho\right) + \frac{\partial}{\partial \eta}\left(h_s u_T \rho\right)\right] + \frac{\partial(u_n \rho)}{\partial \zeta} = 0 \tag{14}$$

$$\frac{\partial u_s}{\partial t} + \frac{u_s}{h_s}\frac{\partial u_s}{\partial \xi} + \frac{u_T}{h_T}\frac{\partial u_s}{\partial \eta} + \frac{u_T u_s}{h_s h_T}\frac{\partial h_s}{\partial \eta} - \frac{u_T^2}{h_s h_T}\frac{\partial h_T}{\partial \xi} = -\frac{1}{\rho h_s}\frac{\partial p}{\partial \xi} \tag{15}$$

$$\frac{\partial u_T}{\partial t} + \frac{u_s}{h_s}\frac{\partial u_T}{\partial \xi} + \frac{u_T}{h_T}\frac{\partial u_T}{\partial \eta} + \frac{u_T u_s}{h_s h_T}\frac{\partial h_s}{\partial \xi} - \frac{u_s^2}{h_s h_T}\frac{\partial h_s}{\partial \eta} = -\frac{1}{\rho h_T}\frac{\partial p}{\partial \eta} \tag{16}$$

$$\frac{\rho}{a^2}\left(\frac{u_s^2}{R_s} + \frac{u_T^2}{R_T}\right) = \frac{1}{a^2}\frac{\partial p}{\partial n} = \frac{\partial \rho}{\partial n} \tag{17}$$

Equations (14) to (17) have been obtained with the isentropic assumption in which a^2 is the square of the speed of sound. By eliminating the space and time derivatives of the density between equations (14) and (17) and replacing the general curvilinear coordinates ξ, η, and ζ with the local s, τ, and n, the following condition on the normal derivatives of the normal velocity is obtained (ref. 3):

$$\rho \frac{\partial u_n^2}{\partial n^2} + 2 \frac{\partial \rho}{\partial n} \frac{\partial u_n}{\partial n} = - \left[\frac{\partial^2 (u_s \rho)}{\partial s\, \partial n} - \frac{1}{R_S} \frac{\partial (u_s \rho)}{\partial s} + \frac{\partial^2 (u_\tau \rho)}{\partial \tau\, \partial n} - \frac{1}{R_\tau} \frac{\partial (u_\tau \rho)}{\partial \tau} + \frac{\partial}{\partial n} \left(\frac{u_s \rho}{R_S} + \frac{u_\tau \rho}{R_\tau} \right) \right.$$

$$\left. + \left(\frac{u_s^2}{R_S} + \frac{u_\tau^2}{R_\tau} \right) \left(\frac{2 - \gamma}{a^2} \right) \frac{\partial \rho}{\partial t} + 2 \left(\frac{u_s}{R_S} \frac{\partial u_s}{\partial t} + \frac{u_\tau}{R_\tau} \frac{\partial u_\tau}{\partial t} \right) \frac{\rho}{a^2} \right] \qquad (18)$$

By center differencing the normal first and second derivatives of the normal velocity, an approximation is obtained to u_n^- on the auxiliary point correct to order $(\delta n)^3$ if the right-hand side of equation (18) can be approximated with an error no greater than $O(\delta n)$. Thus, on the surface of the body, equations (14), (15), and (16) have to be solved while a boundary condition is applied for u_n using equation (18). Note also that the radii of curvature of the surface R_S and R_τ are required for this accurate determination of u_n^-. The second normal derivative of the normal velocity is rigorously required for a second-order-accurate boundary condition, the expression for u_n^- being

$$u_n^- = -u_n^+ + O\left[(\delta n)^2 \frac{1}{R} \right] \qquad (19)$$

However, for mildly curving shapes with $1/R$ of order δn, a simple reflection of u_n will yield second-order accuracy without the complication of introducing the second normal derivative given by equation (18). This simplification is used in the results to be illustrated in the subsequent sections.

UPSTREAM, DOWNSTREAM BOUNDARY CONDITIONS

For a steady-state one-dimensional duct flow, one is not free to specify the downstream boundary conditions if the upstream conditions are fully specified. This is not so in a transonic multidimensional duct flow. In this case the upstream conditions may be set. However, one can still vary a single downstream variable such as the pressure and achieve different steady-state solutions. This degree of freedom on downstream pressure arises because the oblique shock waves present on the blades in the transonic regime are free to move and alter their strength in response to the different downstream pressure conditions. This range of freedom on downstream pressure is limited. It ceases, for example, if the downstream pressure is set high enough so that the shocks are blown forward out of the cascade.

In the actual calculation, boundary conditions were set so that the mean flow at the inlet plane to the duct was held fixed. Waves generated by the rotor which moved upstream into the inlet plane were then allowed to escape. This escape condition was

formulated as an axially one-dimensional characteristics construction at the inlet plane of the computational domain. At the downstream exit plane the pressure was held fixed and the remaining flow variables forced to take a zero axial gradient condition. This condition allows the mean flow velocity at the exit to adjust itself to the correct mass flow; however, it distorts the structure imposed by the rotor locally in the vicinity of the exit plane. This distortion is a consequence of the condition of uniformity of flow in the axial direction rather than in the streamline direction (which is helical rather than axial).

COMPUTATIONAL IMPLEMENTATION

The geometry of the flow field for an illustrative transonic rotor calculation is shown in figures 4 and 5. On the conical spinner are attached $N = 23$ blades with an average hub to tip ratio of 0.6. Thus the flow field of a blade element is bounded by the machine outer and inner casings in the radial direction and by two surfaces $\theta_1(r,z)$ and $\theta_2(r,z)$ in the angular direction such that

$$\theta_2(r,z) - \theta_1(r,z) = \Delta\theta$$

$$\Delta\theta \equiv \frac{2\pi}{N} \tag{20}$$

Let $r_H(z)$ and $r_T(z)$ be the equations of the inner casing (hub) and the outer casing (tip) surfaces. If $\theta = \theta_s(r,z)$ and $\theta = \theta_p(r,z)$ are the equations of the blade suction and pressure surfaces, respectively, then the computational domain boundary surfaces θ_1 and θ_2 may be constructed by making $\theta_1 = \theta_s$ and $\theta_2 = \theta_p$ in the blade region and then extending these surfaces upstream and downstream as ruled surfaces parallel to the machine axis as shown in figure 4.

The complex geometry formed by the extended blade and casing surfaces may be handled computationally by carrying out the computational work in a computational domain $x'_i = (r', \theta', z')$ obtained as a mapping of the physical domain $x_i = (r,\theta,z)$. The complex turbomachine surfaces should map into planar surfaces in the computational domain. Mapping functions selected for this purpose are

$$r' = \frac{r - r_H(z)}{r_T - r_H(z)} r_T \tag{21}$$

$$\theta' = \frac{\theta - \theta_1(r,z)}{\theta_2(r,z) - \theta_1(r,z)} \Delta\theta \tag{22}$$

$$z' = z \tag{23}$$

The Jacobian derivatives of this transformation $g_{ij} = \dfrac{\partial x_i'}{\partial x_j}$ appear in the conservation laws (eq. (1)) so that $\dfrac{\partial F_i}{\partial x_i}$ is replaced by $g_{ij}\dfrac{\partial F_i}{\partial x_j'}$. Similarly, the difference operator (eq. (5)) in the computation domain becomes

$$\underline{U}^* = -\frac{1}{r(r',z')}\left[g_{ij}\frac{\delta t}{\delta x_j'}\Delta_j^+ \underline{F}_i(\underline{U}) + \delta t \underline{K}(\underline{U}) \right]$$

$$S\underline{U} = \frac{1}{2}\left\{ \underline{U}^* + \underline{U} - \frac{1}{r(r',z')}\left[g_{ij}\frac{\delta t}{\delta x_j'}\Delta_j^- \underline{F}_i(\underline{U}^*) + \delta t \underline{K}(\underline{U}^*) \right] \right\} \tag{24}$$

In addition, the blade boundary conditions which require the normal derivatives in the physical domain must be expressed in terms of computational domain coordinates. If ν_i denotes the three direction cosines of the blade surface normal, then the first normal derivative expressed in computational domain coordinates x_j' is

$$\frac{\partial}{\partial n} = \nu_i g_{ij}\frac{\partial}{\partial x_j} \tag{25}$$

and the second normal derivative is

$$\frac{\partial^2}{\partial n^2} = \nu_i \nu_k g_{ij}\frac{\partial}{\partial x_j'} g_{kl}\frac{\partial}{\partial x_l'} \tag{26}$$

The derivative forms (eqs. (25) and (26)) and similar forms for the s and τ derivatives replace those of equations (14) to (18) allowing finite differences to be taken in terms of computational domain coordinates x_j'.

INITIAL RESULTS FOR A TRANSONIC ROTOR

Some initial results obtained with the foregoing method for the single-stage transonic rotor shown in figure 1 are now presented. This rotor operates with a tip Mach number M_T of 1.2 and an average axial Mach number M_a of 0.5. The calculation

illustrated here is for an open throttle situation in which the static pressure behind the rotor remains at a low value relative to the full load design values of the rotor.

The calculation was performed on an IBM 370/168 system. Although this machine has a large primary memory capacity, economic considerations necessitated the use of the secondary memory units for the storage of the U^n and U^{n+1} arrays. Continuous input-output operations between the core and the secondary memory units were required for the calculation.

The computational domain shown in figures 4 and 5 was discretized with 67 points in the axial direction, 30 of which are in the region of the blade. The radial direction was discretized with 12 points, the angular direction with 10 points. This discretization was selected as being the minimum number of points which would provide a representative although not detailed resolution of the flow field. Considerations of economy dictated the use of such a coarse mesh in a developmental calculation such as the one described here. Future calculations may be carried out with expanded mesh densities.

Before going into the details of the obtained results, it might be useful for the reader to familiarize himself with the nature of the coordinate transformation and especially with the shape of the r' = Constant and θ' = Constant surfaces in the physical space. The r' = Constant surfaces are cylindrical surfaces as indicated in figure 5, ranging between the hub and the tip. Actually the tip and the hub surfaces belong to the r' = Constant family of surfaces. The θ' = Constant surfaces are more complicated and, as it can be seen in figure 4, they have no degree of symmetry. However, it is quite apparent that these surfaces are more geometrically related to the blade shape than the θ = Constant planes. Thus, some of the plots of the field properties have been made in the r', θ', and z' coordinate system rather than the r, θ, and z system to improve their clarity.

In figure 6, the Mach number distribution is plotted in r and z coordinates along the span on the θ' = Constant surface that passes at the suction surface of the blade ($\theta' = \Delta\theta$).

There is a strong shock wave originating from the trailing edge of the blade; on the other hand, there is hardly any trace of the leading-edge oblique shock. The flow upstream of the blade varies almost linearly from subsonic close to the hub to supersonic at the tip, as expected, due to the solid body rotation of the flow in the rotary frame.

Because of the wide open throttle condition, the flow accelerates near the hub to a higher Mach number (approximately 1.9 compared to 1.6 at the tip). This causes the shock wave at the trailing edge to be strongest near the hub. The flow at the supersonic tip is relatively smooth, the trailing-edge shock decelerating the flow from a Mach number of 1.6 to 1.3.

In figure 7, a similar plot of the Mach number distribution on the pressure side of the blade is illustrated. The effect of the hub geometry becomes more apparent now since the flow on the pressure side is accelerating. The maximum Mach number on the pressure side is 1.55 and occurs at the tip section. A shock is present also on the pressure side; however, its strength is diminishing towards the hub, where the flow becomes nearly sonic. The pressure side shock appears upstream of the trailing edge and, as will become apparent in the next figures, it extends to the trailing edge of the suction side of the adjacent blade.

In figures 8 and 9, the intersections of the sonic surface with the pressure and the suction side have been traced in r and z coordinates. In figure 8, corresponding to the pressure side ($\theta = 0$), the presence of the trailing-edge shock is rather apparent. This shock is normal to the hub surface at the pressure side, changing to an oblique towards the suction side (fig. 9). In figures 10, 11, and 12, the Mach number contours have been plotted in θ and z coordinates on the three $r' = $ Constant cylinders corresponding to the tip, mid, and hub sections of the blade. The location and the strength of the trailing-edge shock can now be easily established.

Figures 13 and 14 show the pressure coefficient

$$C_p = \frac{p - p_\infty}{\rho_\infty a_\infty^2}$$

(where $(\ )_\infty$ indicates the properties far upstream) on the suction and pressure sides at typical blade sections near the tip and the hub, respectively. The location of the trailing-edge shock can be easily established on both blade surfaces.

In figure 13, the leading-edge shock can be clearly identified. This shock appears to be stronger on the suction side of the blade. At the pressure side near the trailing edge, there is evidence of an expansion fan that matches the local static pressure at the two sides of the blade. With respect to the blade's lift distribution along the span, the tip section produces little work at the open throttle condition; on the other hand, the hub sections are working very hard, but in vain, in view of the strong shock at the trailing edge that dissipates much of the stagnation pressure rise produced at the hub.

In figure 15 is plotted the distribution of the crossflow velocity u_r on the $\theta = $ Constant surface that passes at the blade's suction surface ($\theta = \Delta\theta$). The behavior of u_r is generally determined by the shape of the hub and tip; however, in the region around the trailing edge of the blade, the appearing shock has a significant effect. Due to the acceleration of the flow, the pressure upstream of the shock is lower at the hub than at the tip; thus, a crossflow is developed from the tip to the hub. On the contrary, downstream of the shock, the crossflow reverses direction because now the hub pressure is higher since the shock is stronger at the hub.

Figures 13 and 14 also clearly show the acceleration of the flow, even in the supersonic region near the blade tips, due to the influence of the subsonic zone near the hub. This is a crucial effect in such a genuinely mixed flow; for even though axially propagating signals cannot influence the supersonic zone, it is possible for disturbances to feed back upstream through the subsonic zone and then radially impact the upstream supersonic flow at the tip.

REFERENCES

1. MacCormack, Robert W.: Numerical Solution of the Interaction of a Shock Wave With a Laminar Boundary Layer. Proceedings of the Second International Conference on Numerical Methods in Fluid Dynamics. Vol. 8 of Lecture Notes in Physics, Maurice Holt, ed., Springer-Verlag, 1971, pp. 151-163.

2. MacCormack, R. W.; and Paullay, A. J.: Computational Efficiency Achieved by Time Splitting of Finite Difference Operators. AIAA Paper No. 72-154, Jan. 1972.

3. Sparis, P.: A Computational Study of the Three Dimensional Flow in a Single Stage Transonic Compressor. Ph. D. Thesis, Massachusetts Inst. Technol., 1974.
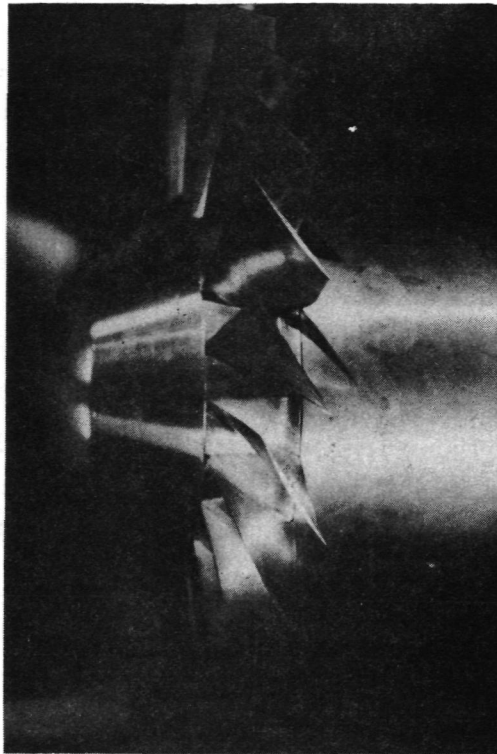
Figure 1.- Single stage transonic compressor rotor designed with average hub-tip radius ratio of 0.6; axial Mach number, 0.5; tip Mach number, 1.2.
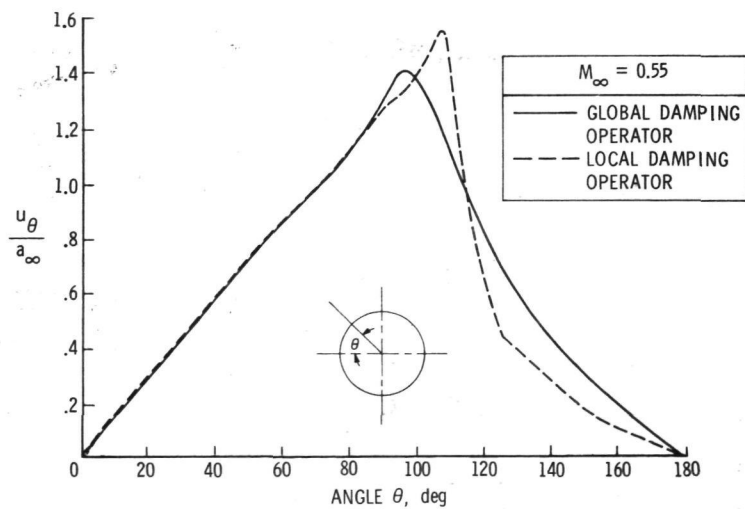
Figure 2.- Test of local damping operator $D(M)$ for transonic flow of $\gamma = 1.4$ gas over right circular cylinder. Twenty points distributed over θ.
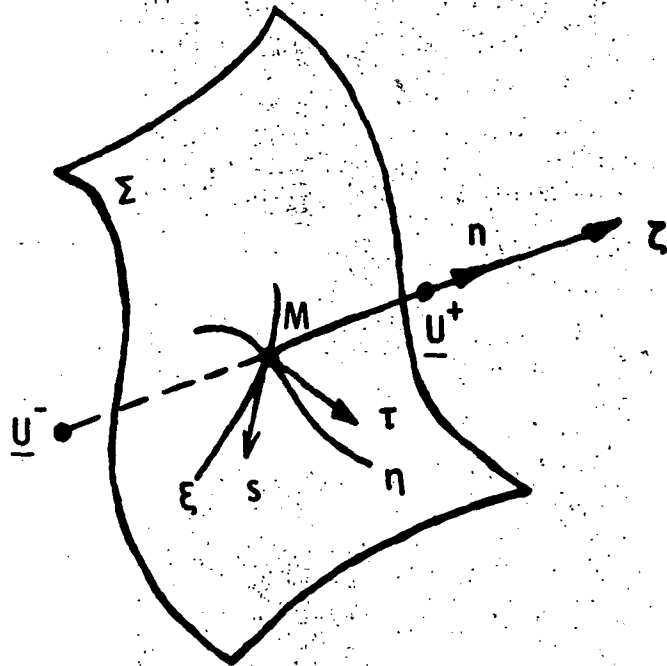
Figure 3.- Surface geometry.
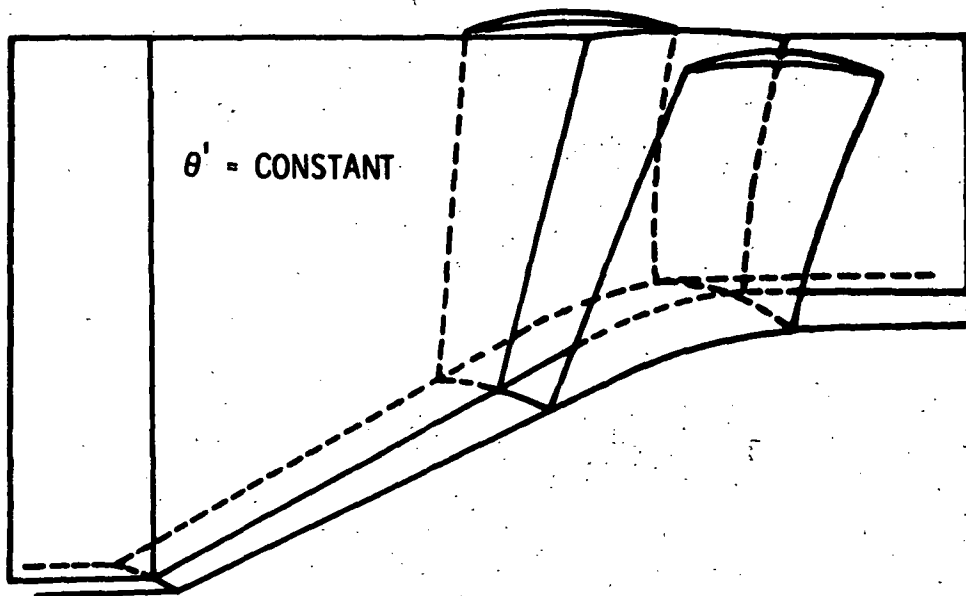
Figure 4.- Computational domain (passage view) illustrating blades and $\theta' =$ Constant surface.

12   52 62
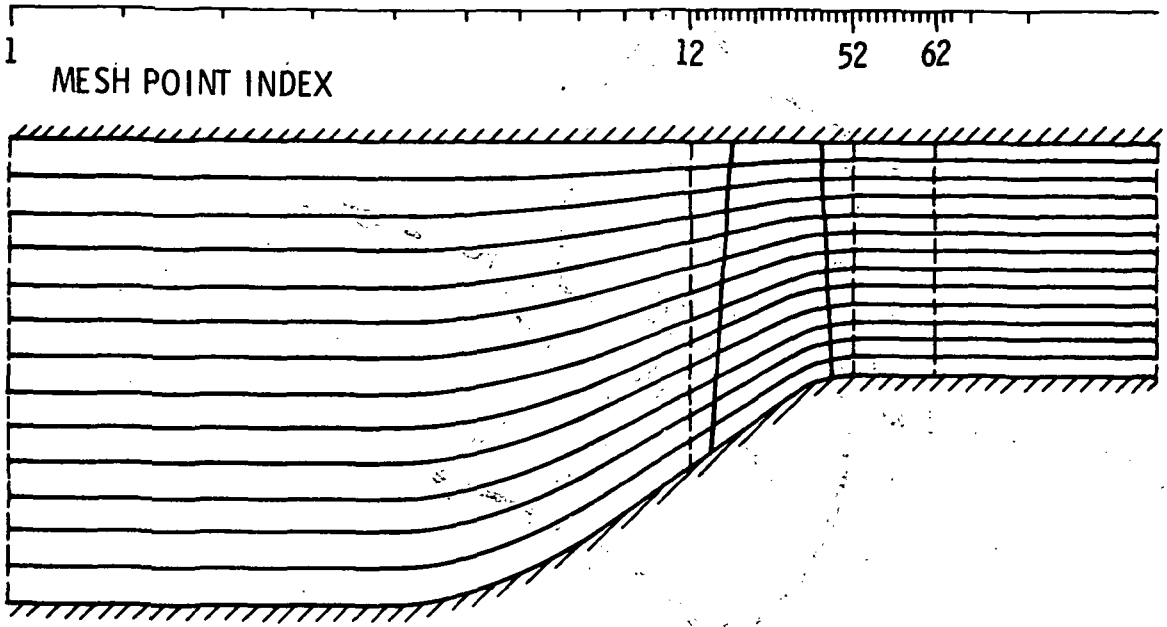
Figure 5.- Computational domain (section view) along axis of machine illustrating r' = Constant surfaces.
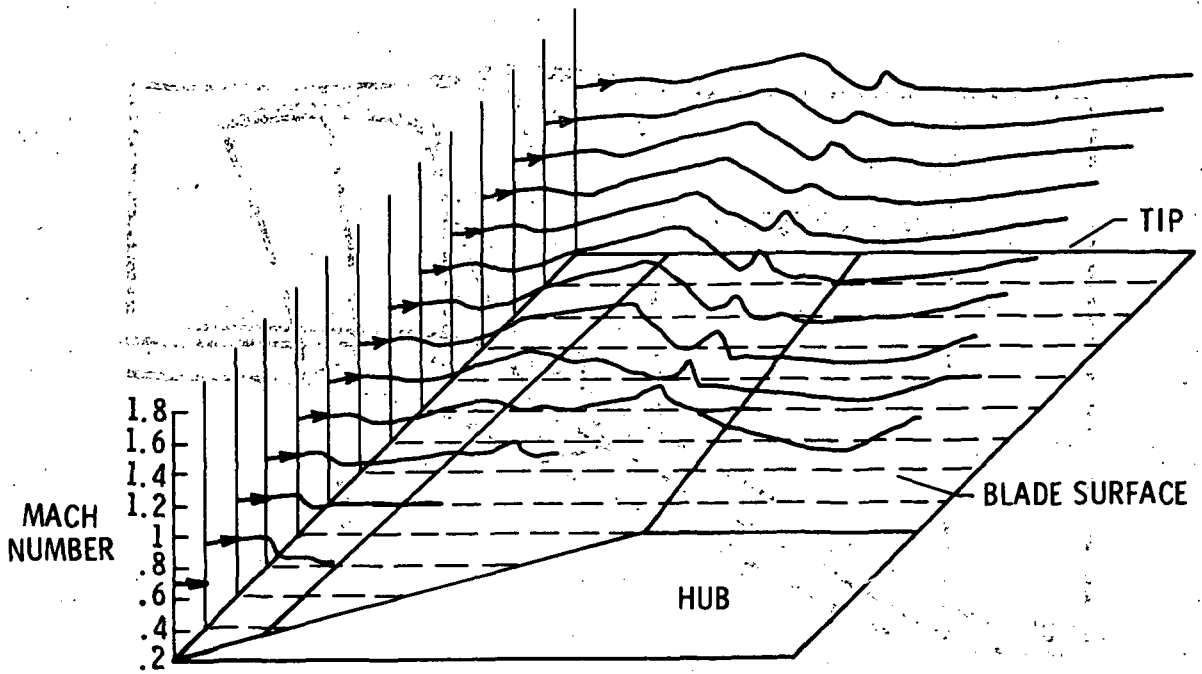
Figure 6.- Mach number distribution over blade surface (suction side).
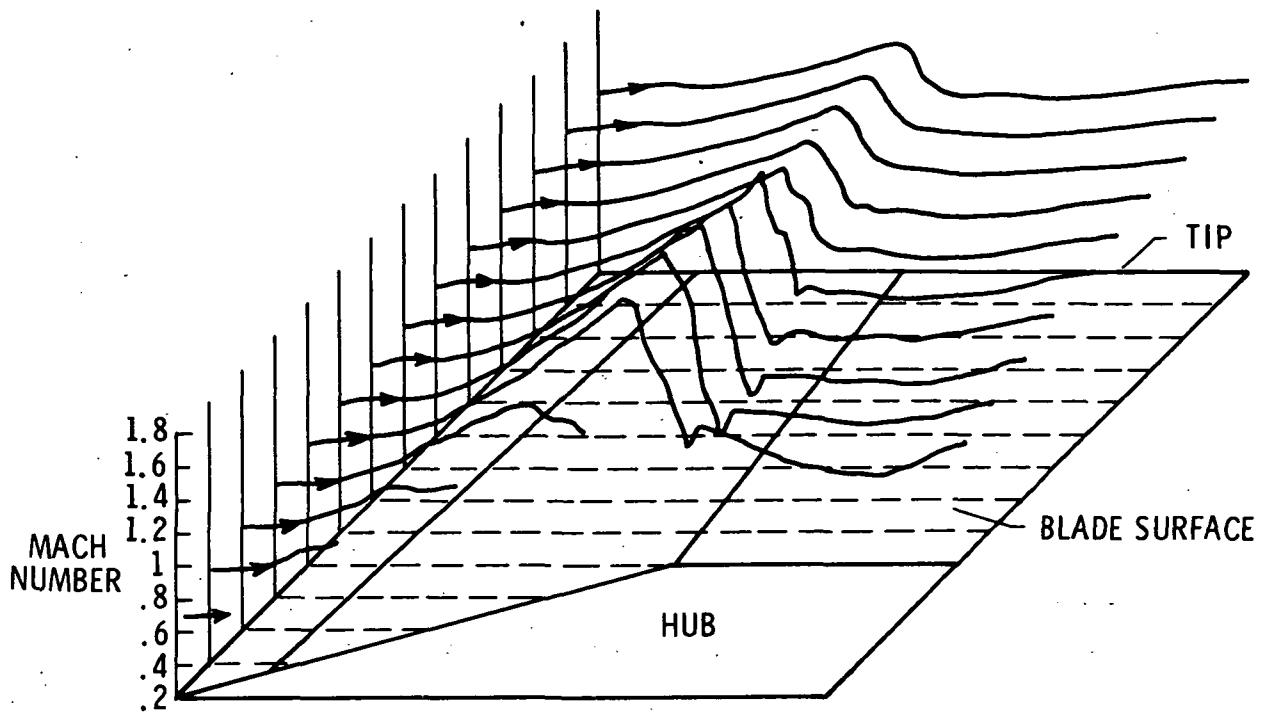
Figure 7.- Mach number distribution over blade surface (pressure side).
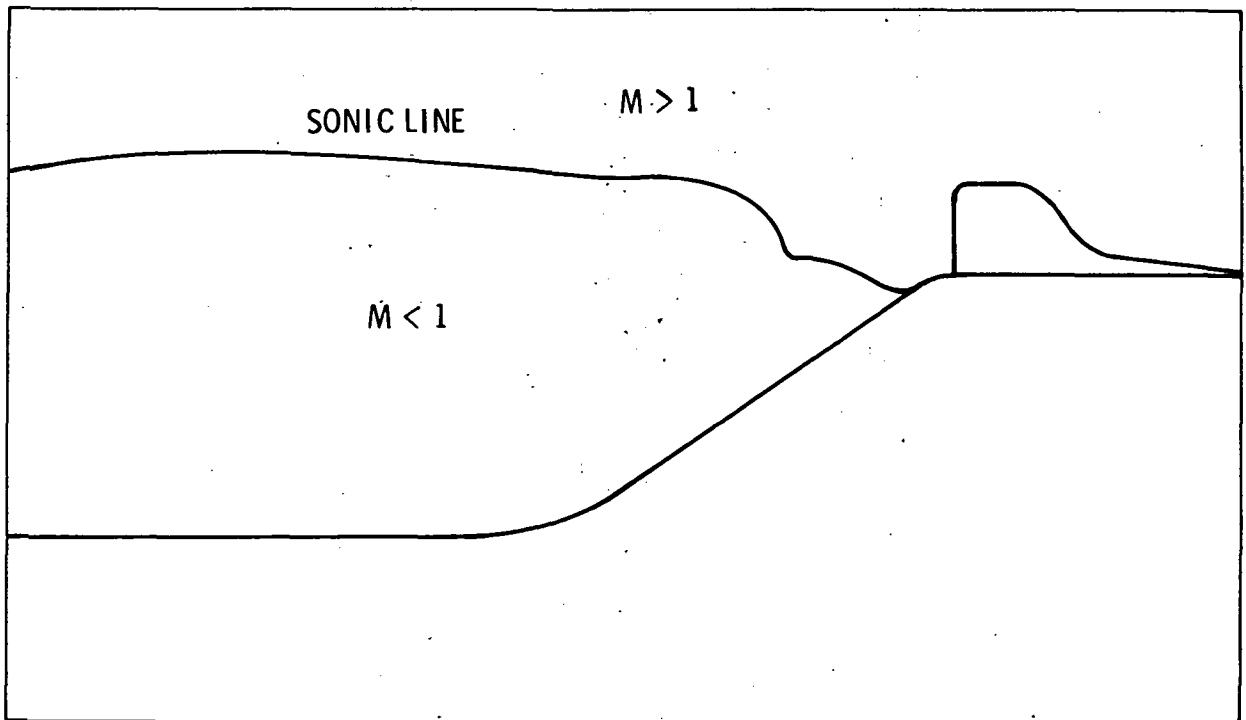
Figure 8.- Sonic surface intersections with $\theta = \theta_1$ surface (pressure side).
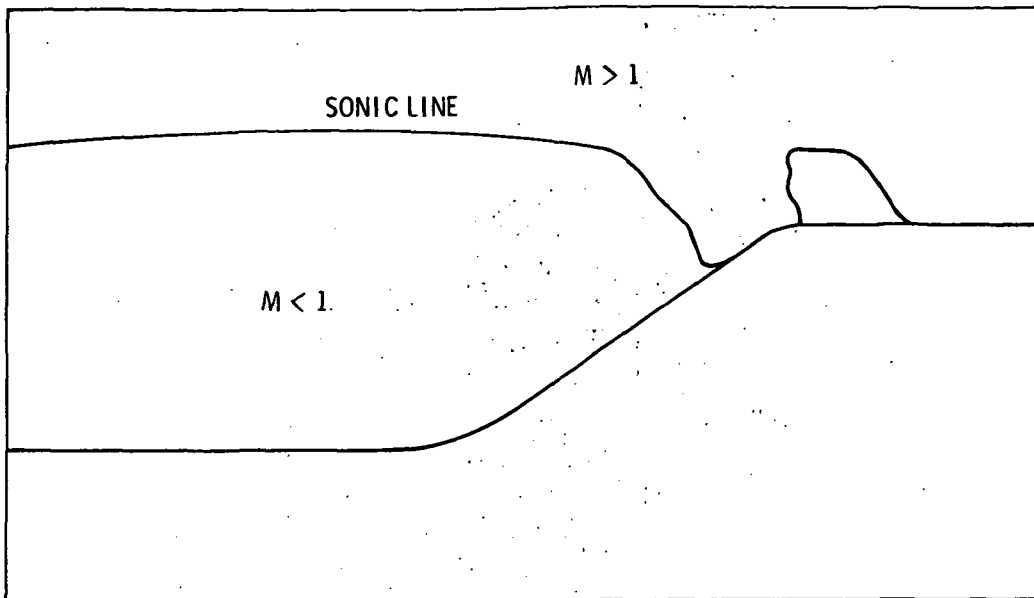
Figure 9.- Sonic surface intersections with $\theta = \theta_2$ surface (suction side).
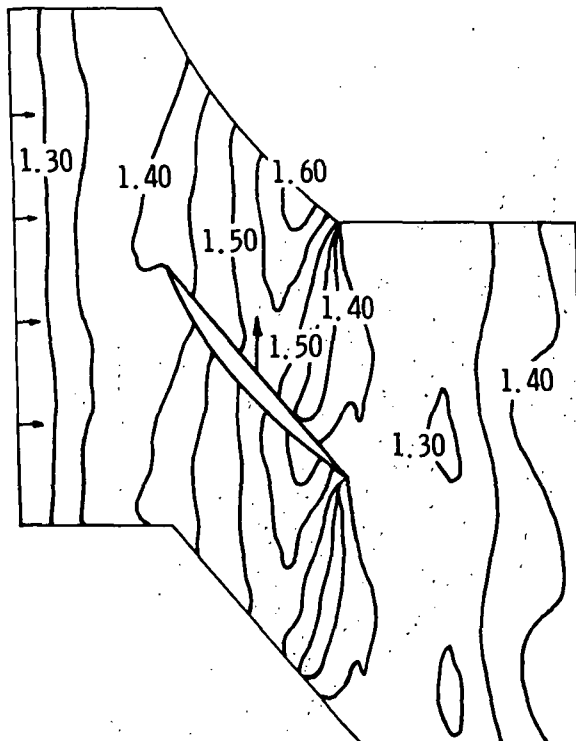
Figure 10.- Mach number contours in interblade region along
$r' = $ Constant surface (tip section).
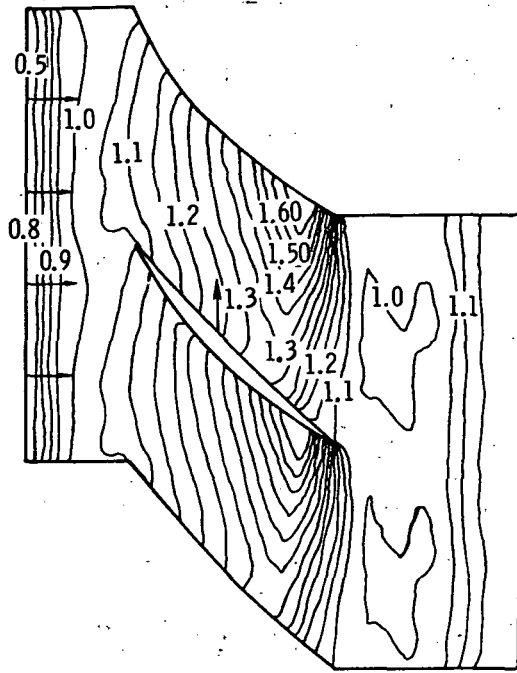
Figure 11.- Mach number contours in interblade region along
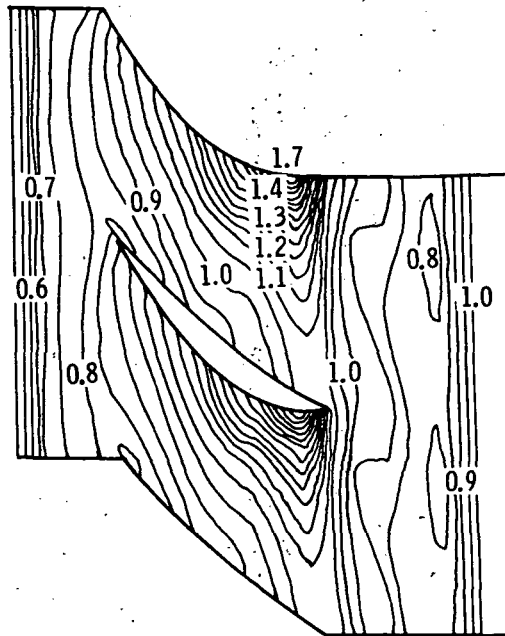r' = Constant surface (midspan section).

Figure 12.- Mach number contours in interblade region along
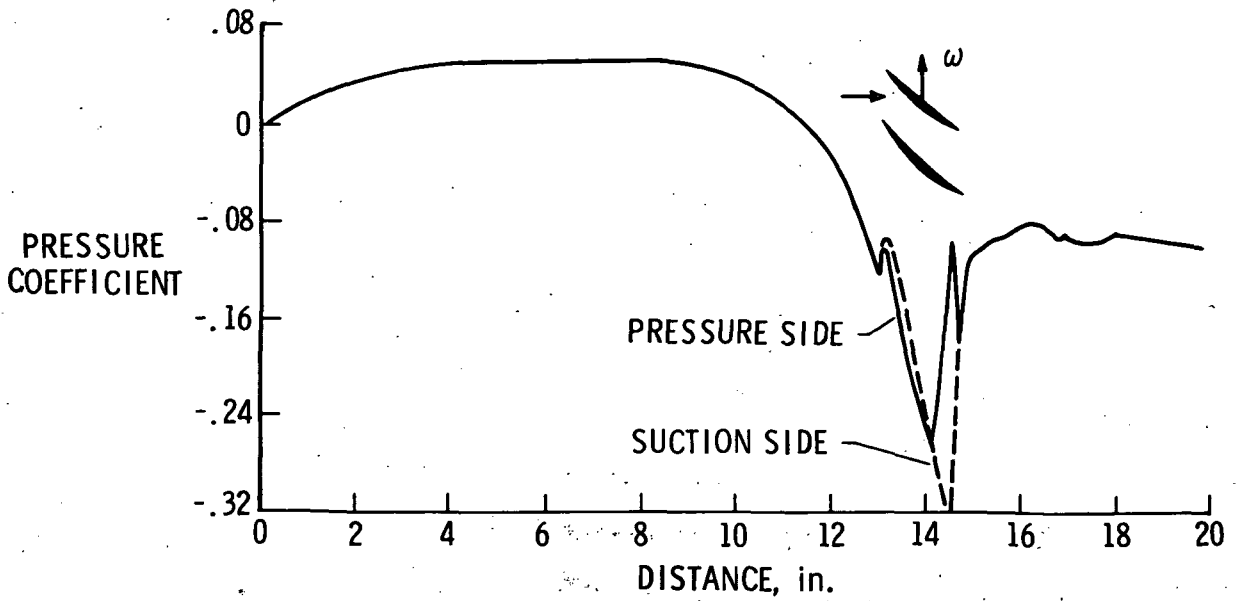r' = Constant surface (hub section).

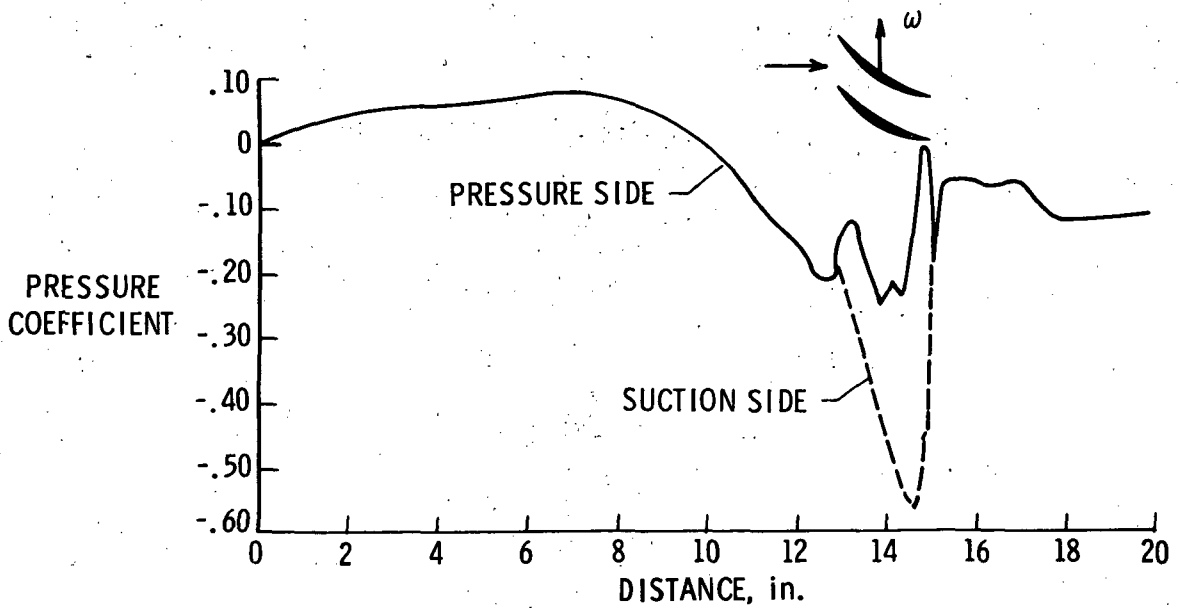Figure 13.- Pressure coefficient through passage and over blades at tip.
(1 in. = 2.54 cm.)

Figure 14.- Pressure coefficient through passage and over blades at hub.
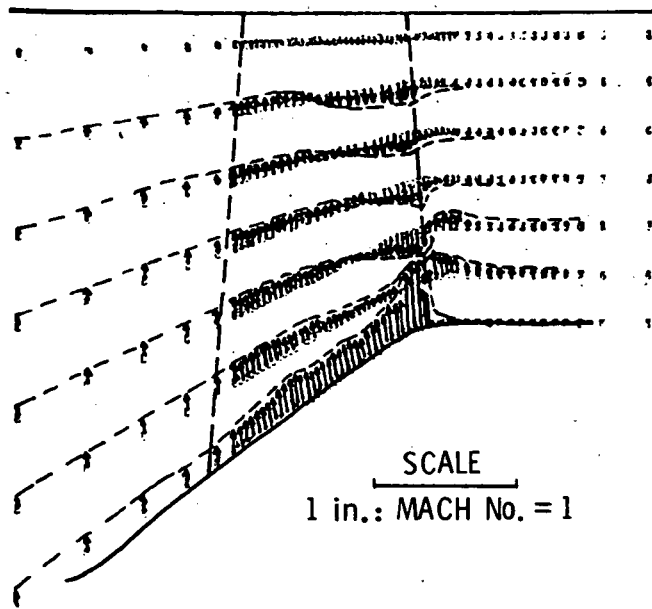(1 in. = 2.54 cm.)

SCALE

1 in.: MACH No. = 1

Figure 15.- Crossflow velocity u_r distributions.